Simulation of a Turbulent Impinging Jet into a Layer of Porous Material Using a Two-Energy Equation Model

Marcelo J. S. de Lemos [a] & Felipe T. Dórea

[a] Departamento de Energia—IEME , Instituto Tecnológico de Aeronáutica—ITA, São José dos Campos , São Paulo, Brazil
Published online: 31 May 2011.

PLEASE SCROLL DOWN FOR ARTICLE

Taylor & Francis
Taylor & Francis Group

SIMULATION OF A TURBULENT IMPINGING JET INTO A LAYER OF POROUS MATERIAL USING A TWO–ENERGY EQUATION MODEL

Marcelo J. S. de Lemos and Felipe T. Dórea
Departamento de Energia—IEME, Instituto Tecnológico de Aeronáutica—ITA, São José dos Campos, São Paulo, Brazil

This article presents numerical results for a turbulent jet impinging against a flat plane covered with a layer of permeable and thermally conducting material. Distinct energy equations are considered for the solid porous material attached to the wall and for the fluid that impinges on it. Parameters such as Reynolds number, porosity, permeability, thickness, and thermal conductivity of the porous layer are varied in order to analyze their effects on the local distribution of Nu. The macroscopic equations for mass, momentum, and energy are obtained based on volume-average concept. The numerical technique employed for discretizing the governing equations was the control volume method with a boundary-fitted nonorthogonal coordinate system. The SIMPLE algorithm was used to handle the pressure-velocity coupling. Results indicate that inclusion of a porous layer eliminates the peak in Nu at the stagnation region. For highly porous and highly permeable material, simulations indicate that the integral heat flux from the wall is enhanced when a thermally conducting porous material is attached to the surface.

1. INTRODUCTION

Impinging jets are often used in industrial applications for enhancing or damping localized heat transfer rates. When the flow is turbulent, thin boundary layers are located inside the stagnation zone, promoting even further cooling, heating or drying processes. Applications of such systems include metals cooling, glass tempering, electronics cooling, and drying of textiles products and paper, to mention a few.

The majority of results in the open literature are mostly related to impinging jets under high mass flow conditions that reach a bare surface. Studies considering two-dimensional impinging jets with low Reynolds number, also onto uncovered walls, are presented in Gardon and Akfirat [1], who experimentally obtained local and averaged heat transfer coefficients. Sparrow and Wong [2] made use of the well-known heat and mass transfer analogy and took experimental data on local mass transfer for a two-dimensional impinging jet. Results were then converted to

NOMENCLATURE

A_i	interstitial area between phases		Re	Reynolds number based on the jet
B	jet width			width, $Re = \rho v_0 B / \mu$
c_F	Forchheimer coefficient		S	source term
Da	Darcy number, $Da = K/H^2$		T	temperature
H	channel height		$\langle u \rangle^i$	intrinsic (fluid) average of u
h	porous layer thickness, film coefficient		u_D	Darcy velocity vector (volume average over $u) = \phi \langle u \rangle^i$
K	permeability		x, y	Cartesian coordinates
k_{eff}	effective thermal conductivity		μ	dynamic viscosity
k	thermal conductivity		ρ	density
L	channel length		v	kinematic viscosity
Nu	nusselt number			
p	thermodynamic pressure		**Subscripts**	
q_w	integral wall heat flux		s, f	solid, fluid
q_w^ϕ	integral wall heat flux with porous layer		w	wall
			ϕ	related to porous medium
$\langle p \rangle^i$	intrinsic (fluid) average of pressure p		o	inlet conditions

heat transfer using the mentioned technique. Chen et al. [3] experimentally and numerically analyzed mass and heat transfer induced by a two-dimensional laminar jet. Chiriac and Ortega [4] performed numerical simulations in steady and transitory regime for a two-dimensional jet impinging against a plate with constant temperature. Additional works on impinging jets on bare surfaces for oscillating [5] and steady-state regimes are also found in the literature [6–8].

In addition, recently a number of research papers covered a wide range of studies in porous media [9–25], including flows parallel to a layer of porous material [26], across permeable baffles [27, 28] and through porous inserts [29]. Investigation on configurations concerning perpendicular jets into a porous core is needed for optimization of heat sinks attached to solid surfaces. However, studies of porous medium under impinging jets are, unfortunately, very scarce in the literature. An example found is given by the numerical simulations of Kim and Kuznetsov [30], who investigated optimal characteristics of impinging jets into heat sinks. Other innovative applications of impinging jets, such as fiber hydroentalglement, can also be found in the recent literature [31, 32].

Additional examples of work on impinging jets are presented by Prakash et al. [33, 34], who obtained a flow visualization of turbulent jets impinging against a porous medium. Also, Fu and Huang [35] evaluated the thermal performance of different porous layers under a impinging jet, and Jeng and Tzeng [36] studied the hydrodynamic and thermal performance of a jet impinging on a metallic foam. Recently, the flow structure of a jet impinging on a porous layer has been investigated for both laminar [37] and turbulent [38] regimes. In reference [38], the turbulence model described in detail by reference [39] was applied. Earlier, Rocamora and de Lemos [40] had added thermal modeling considering thermal equilibrium between the solid and the fluid. Later, the work on isothermal impinging jets was extended to involve laminar [41] as well as turbulent [42] thermal analyses, which were based on the local thermal equilibrium hypothesis (LTE) [40]. Subsequently, the one-energy equation

model of reference [40] was extended to account for energy transport in each phase, using, for achieving such goal, the so-called local thermal-nonequilibrium model (LTNE). The LTNE closure was then applied to both flow regimes, namely laminar [43] and turbulent [44] flows. More recently, the local nonthermal equilibrium model was applied to simulate a laminar impinging jet into a porous layer [45].

The objective of the present study is to extend the thermal analysis of reference [45], which was limited to laminar flow only, to a fully turbulent regime in order to evaluate the use of the LTNE model in predicting impinging jets into a porous material. By that, one can exploit the advantages, if any, in adding a layer of porous material to enhance the overall heat transferred from a surface.

Whenever possible, comparisons with the local thermal equilibrium hypothesis (LTE) are presented. In the text to follow, the LTE model is also given the acronym 1EEM, for one-energy equation model, whereas the LNTE approach is recalled as 2EEM, two-energy equation model.

2. GEOMETRY

The cases considered here are detailed in Figure 1a. A turbulent jet with uniform velocity v_o and constant temperature T_o enters through a gap into a channel with height H and length $2L$. Fluid impinges normally against the bottom plate yielding a two-dimensional confined impinging jet configuration. The width of the inlet nozzle is B and the bottom plate temperature, T_1, is maintained constant and 38.5 K above the temperature of the incoming jet, T_o. In a different configuration, the bottom surface is covered with a porous layer of height h (Figure 1b). In both cases, the flow is assumed to be two-dimensional, turbulent, incompressible, and steady. Also, the porous medium is taken to be homogeneous, rigid, and inert. Fluid properties are constant and gravity effects are neglected.

The boundary conditions for the problem are: 1) constant velocity and temperature profiles of the entering jet, 2) no slip condition on the walls, 3) symmetry condition in $x = 0$, and 4) fully developed flow at channel exit $(x = L)$. At the bottom plate $(y = H)$, a constant temperature condition is assumed whereas along the upper wall, for $B/2 < x \leq L$, null heat flux condition prevails.

3. FLOW AND HEAT TRANSFER MODELS

As the flow model employed here is already described in Graminho and de Lemos [38], in addition to thermal modeling using one- [40] and two-energy [44] equation closures, macroscopic governing equations will only be presented as most of the theoretical development is readily available in the open literature. As such, details about their derivations can be obtained in the aforementioned papers. In this technique, local instantaneous equations are time-and volume-averaged using appropriate mathematical tools [46], briefly described in the next section.

Macroscopic Flow Equations

When both time- and volume-averaged operations are simultaneously applied to the local instantaneous flow equations, over a representative elementary volume (REV), the following is obtained [39].
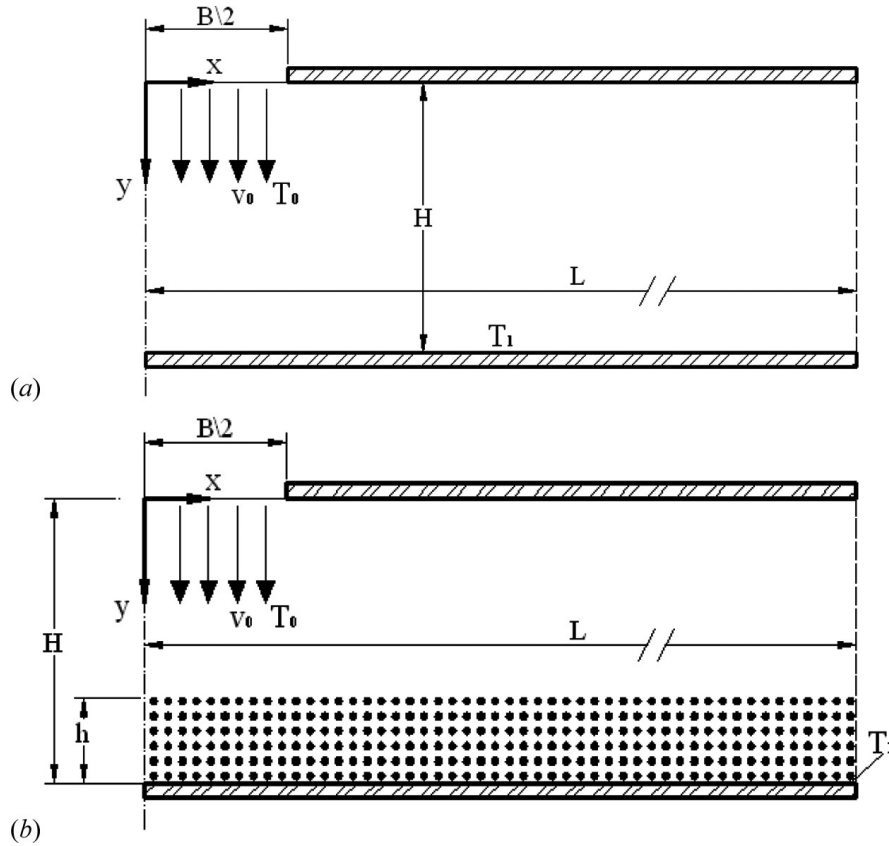
Figure 1. Cases investigated. (*a*) Confined impinging jet on a flat plate—clear medium case; and (*b*) confined impinging jet on a plate covered with a layer of porous material—porous case.

Continuity

$$\nabla \cdot \bar{\mathbf{u}}_D = 0 \tag{1}$$

where $\bar{\mathbf{u}}_D = \phi\langle\bar{\mathbf{u}}\rangle^i$ and $\langle\bar{\mathbf{u}}\rangle^i$ identifies the intrinsic (liquid) average of the time-averaged velocity vector $\bar{\mathbf{u}}$.

Momentum

$$\rho\left[\frac{\partial\bar{\mathbf{u}}_D}{\partial t} + \nabla \cdot \left(\frac{\bar{\mathbf{u}}_D\bar{\mathbf{u}}_D}{\phi}\right)\right] = -\nabla(\phi\langle\bar{p}\rangle^i) + \mu\nabla^2\bar{\mathbf{u}}_D - \nabla \cdot (\rho\phi\langle\overline{\mathbf{u}'\mathbf{u}'}\rangle^i)$$
$$- \left[\frac{\mu\phi}{K}\bar{\mathbf{u}}_D + \frac{c_F\phi\rho|\bar{\mathbf{u}}_D|\bar{\mathbf{u}}_D}{\sqrt{K}}\right] \tag{2}$$

where the last two terms in Eq. (2) represent the Darcy, or viscous, and Forchheimer, or form, drags. The symbol K is the porous medium permeability, c_F is the form drag or Forchheimer coefficient, $\langle\bar{p}\rangle^i$ is the intrinsic average pressure of the fluid, and ϕ is the porosity of the porous medium.

The macroscopic Reynolds stress, $-\rho\phi\langle\overline{\mathbf{u}'\mathbf{u}'}\rangle^i$, appearing in Eq. (2) is given as,

$$-\rho\phi\langle\overline{\mathbf{u}'\mathbf{u}'}\rangle^i = \mu_{t_\phi}2\langle\overline{\mathbf{D}}\rangle^{\mathbf{v}} - \frac{2}{3}\phi\rho\langle k\rangle^i\mathbf{I} \tag{3}$$

where,

$$\langle\overline{\mathbf{D}}\rangle^v = \frac{1}{2}[\nabla(\phi\langle\overline{\mathbf{u}}\rangle^i) + [\nabla(\phi\langle\overline{\mathbf{u}}\rangle^i)]^T] \tag{4}$$

is the macroscopic deformation tensor, $\langle k\rangle^i = \langle\overline{\mathbf{u}'\cdot\mathbf{u}'}\rangle^i/2$ is the intrinsic turbulent kinetic energy, and μ_{t_ϕ}, is the turbulent viscosity which is modeled similarly to the case of clear flow, in the following form.

$$\mu_{t_\phi} = \rho f_\mu c_\mu \frac{\langle k\rangle^{i^2}}{\langle\varepsilon\rangle^i} \tag{5}$$

The intrinsic turbulent kinetic energy per unit mass and its dissipation rate are governed by the following equations.

$$\rho\left[\frac{\partial}{\partial t}(\phi\langle k\rangle^i) + \nabla\cdot(\overline{\mathbf{u}}_D\langle k\rangle^i)\right] = \nabla\cdot\left[\left(\mu+\frac{\mu_{t_\phi}}{\sigma_k}\right)\nabla(\phi\langle k\rangle^i)\right] - \rho\langle\overline{\mathbf{u}'\mathbf{u}'}\rangle^i : \nabla\overline{\mathbf{u}}_D$$
$$+ c_k\rho\frac{\phi\langle k\rangle^i|\overline{\mathbf{u}}_D|}{\sqrt{K}} - \rho\phi\langle\varepsilon\rangle^i \tag{6}$$

$$\rho\left[\frac{\partial}{\partial t}(\phi\langle\varepsilon\rangle^i) + \nabla\cdot(\overline{\mathbf{u}}_D\langle\varepsilon\rangle^i)\right] = \nabla\cdot\left[\left(\mu+\frac{\mu_{t_\phi}}{\sigma_\varepsilon}\right)\nabla(\phi\langle\varepsilon\rangle^i)\right]$$
$$+ c_1(-\rho\langle\overline{\mathbf{u}'\mathbf{u}'}\rangle^i : \nabla\overline{\mathbf{u}}_D)\frac{\langle\varepsilon\rangle^i}{\langle k\rangle^i} \tag{7}$$
$$+ c_2 c_k\rho\frac{\phi\langle\varepsilon\rangle^i|\overline{\mathbf{u}}_D|}{\sqrt{K}} - c_2 f_\mu\rho\phi\frac{\langle\varepsilon\rangle^{i^2}}{\langle k\rangle^i}$$

where $\sigma_k = 1.4$, $\sigma_\varepsilon = 1.3$, $c_1 = 1.50$, $c_2 = 1.90$, and $c_\mu = 0.09$ are constant [47] and f_2 and f_μ are damping functions, given by [48]

$$f_2 = \left\{1 - \exp\left[-\frac{(\nu\varepsilon)^{0.25}n}{3.1\nu}\right]\right\}^2 \times \left\{1 - 0.3\exp\left[-\left(\frac{(k^2/\nu\varepsilon)}{6.5}\right)^2\right]\right\} \tag{8}$$

$$f_\mu = \left\{1 - \exp\left[-\frac{(\nu\varepsilon)^{0.25}n}{14\nu}\right]\right\}^2 \times \left\{1 + \frac{5}{(k^2/\nu\varepsilon)^{0.75}}\exp\left[-\left(\frac{(k^2/\nu\varepsilon)}{200}\right)^2\right]\right\} \tag{9}$$

where n is the coordinate normal to the wall. Constant $c_k = 0.28$ was proposed by de Lemos and his students [40] to handle turbulence in porous media.

Two-Energy Equation Model

Similarly, macroscopic energy equations are obtained for both fluid and solid phases by applying time- and volume-averaged operators to local instantaneous energy equations, resulting in

$$
(\rho c_p)_f \left[\frac{\partial \phi \langle \overline{T_f} \rangle^i}{\partial t} + \nabla \cdot \left\{ \phi \left(\langle \overline{\mathbf{u}} \rangle^i \langle \overline{T_f} \rangle^i + \underbrace{\langle {}^i\overline{\mathbf{u}}^i\overline{T_f} \rangle^i}_{\text{thermal disperson}} + \underbrace{\overline{\langle \mathbf{u}' \rangle^i \langle T_f' \rangle^i}}_{\text{turbulent heat flux}} \right. \right. \right.
$$

$$
\left. \left. \left. + \underbrace{\langle \overline{{}^i\mathbf{u}'\,{}^iT_f'} \rangle^i}_{\text{turbulent thermal dispersion}} \right) \right\} \right] = \nabla \cdot \underbrace{\left[k_f \nabla(\phi \langle \overline{T_f} \rangle^i) + \frac{1}{\Delta V} \int_{A_i} \mathbf{n}_i k_f \overline{T_f} dA \right]}_{\text{conduction}}
$$

$$
+ \underbrace{\frac{1}{\Delta V} \int_{A_i} \mathbf{n}_i \cdot k_f \nabla \overline{T_f} dA}_{\text{interfacial heat transfer}}
$$

$$\tag{10}$$

where the expansion

$$
\langle \overline{\mathbf{u}'T_f'} \rangle^i = \overline{\langle (\langle \mathbf{u}' \rangle^i + {}^i\mathbf{u}')(\langle T_f' \rangle^i + {}^iT) \rangle}^i = \overline{\langle \mathbf{u}' \rangle^i \langle T_f' \rangle^i} + \langle \overline{{}^i\mathbf{u}'\,{}^iT_f'} \rangle^i \tag{11}
$$

has been used in light of the double decomposition concept given in reference [40]. For the solid phase, one has

$$
(\rho c_p)_s \left\{ \frac{\partial (1 - \phi) \langle \overline{T_s} \rangle^i}{\partial t} \right\} = \nabla \cdot \underbrace{\left\{ k_s \nabla [(1 - \phi) \langle \overline{T_s} \rangle^i] - \frac{1}{\Delta V} \int_{A_i} \mathbf{n}_i k_s \overline{T_s} dA \right\}}_{\text{conduction}}
$$

$$
\underbrace{- \frac{1}{\Delta V} \int_{A_i} \mathbf{n}_i \cdot k_s \nabla \overline{T_s} dA}_{\text{interfacial heat transfer}}
$$

$$\tag{12}$$

In Eqs. (10) and (12), $\langle \overline{T_s} \rangle^i$ and $\langle \overline{T_f} \rangle^i$ denote the intrinsic average temperature of solid and fluid phases, respectively, A_i is the interfacial area within the REV, and $\mathbf{n}_i$ is the unit vector normal to the fluid-solid interface, pointing from the fluid towards the solid phase. Equations (10) and (12) are the macroscopic energy equations for the fluid and the porous matrix (solid), respectively.

In order to use Eqs. (10) and (12), the underscored terms have to be modeled in some way as a function of the intrinsically averaged temperature of solid phase and fluid, $\langle \overline{T_s} \rangle^i$ and $\langle \overline{T_f} \rangle^i$. To accomplish this, a gradient type diffusion model is used for all the terms, in the following form.

Turbulent heat flux: $- (\rho c_p)_f (\phi \overline{\langle \mathbf{u}' \rangle^i \langle T_f' \rangle^i}) = \mathbf{K}_t \cdot \nabla \langle \overline{T_f} \rangle^i$ (13)

Thermal dispersion: $- (\rho c_p)_f (\phi \langle {}^i \overline{\mathbf{u}}^i \overline{T_f} \rangle^i) = \mathbf{K}_{\mathrm{disp}} \cdot \nabla \langle \overline{T_f} \rangle^i$ (14)

Turbulent thermal dispersion: $- (\rho c_p)_f (\phi \langle \overline{{}^i \mathbf{u}'{}^i T_f'} \rangle^i) = \mathbf{K}_{\mathrm{disp},t} \cdot \nabla \langle \overline{T_f} \rangle^i$ (15)

Local conduction:
$$\nabla \cdot \left[\frac{1}{\Delta V} \int_{A_i} \mathbf{n}_i k_f \overline{T_f} dA \right] = \mathbf{K}_{f,s} \cdot \nabla \langle \overline{T}_s \rangle^i$$
$$- \nabla \cdot \left[\frac{1}{\Delta V} \int_{A_i} \mathbf{n}_i k_s \overline{T_s} dA \right] = \mathbf{K}_{s,f} \cdot \nabla \langle \overline{T}_f \rangle^i.$$
(16)

In this work, for simplicity, one assumed that for turbulent flow the overall thermal resistance between the two phases is controlled by the interfacial film coefficient, rather than by the thermal resistance within each phase. As such, the tortuosity coefficients $\mathbf{K}_{f,s}$, $\mathbf{K}_{s,f}$ are here neglected for the sake of simplicity.

The heat transferred between the two phases can be modeled by means of a film coefficient h_i such that,

$$h_i a_i (\langle \overline{T_s} \rangle^i - \langle \overline{T_f} \rangle^i) = \frac{1}{\Delta V} \int_{A_i} \mathbf{n}_i \cdot k_f \nabla \overline{T_f} dA = \frac{1}{\Delta V} \int_{A_i} \mathbf{n}_i \cdot k_s \nabla \overline{T_s} dA$$ (17)

where $a_i = A_i / \Delta V$ is the surface area per unit volume.

For the above shown expressions, Eqs. (10) and (12) can be written as:

$$\{(\rho c_p)_f \phi\} \frac{\partial \langle \overline{T_f} \rangle^i}{\partial t} + (\rho c_p)_f \nabla \cdot (\mathbf{u}_D \langle \overline{T_f} \rangle^i) = \nabla \cdot \{\mathbf{K}_{\mathrm{eff},f} \cdot \nabla \langle \overline{T_f} \rangle^i\} + h_i a_i (\langle \overline{T_s} \rangle^i - \langle \overline{T_f} \rangle^i)$$

(18)

$$\{(1 - \phi)(\rho c_p)_s\} \frac{\partial \langle \overline{T_s} \rangle^i}{\partial t} = \nabla \cdot \{\mathbf{K}_{\mathrm{eff},s} \cdot \nabla \langle \overline{T_s} \rangle^i\} - h_i a_i (\langle \overline{T_s} \rangle^i - \langle \overline{T_f} \rangle^i)$$ (19)

where, $\mathbf{K}_{\mathrm{eff},f}$ and $\mathbf{K}_{\mathrm{eff},s}$ are the effective conductivity tensor for fluid and solid, respectively, given by

$$\mathbf{K}_{\mathrm{eff},f} = [\phi k_f]\mathbf{I} + \mathbf{K}_{f,s} + \mathbf{K}_t + \mathbf{K}_{\mathrm{disp}} + \mathbf{K}_{\mathrm{disp},t}$$ (20)

$$\mathbf{K}_{\mathrm{eff},s} = [(1 - \phi)k_s]\mathbf{I} + \mathbf{K}_{s,f}$$ (21)

and $\mathbf{I}$ is the unit tensor.

One Energy Equation Model

For the sake of comparison, we present here the energy equation using the local thermal equilibrium hypothesis (LTE, $\langle \overline{T_f} \rangle^i = \langle \overline{T_s} \rangle^i = \langle \overline{T} \rangle^i$), which has been given in detail in the work of Fischer and de Lemos [42], and consists in adding

Eqs. (18) and (19) as follows.

$$\{(\rho c_p)_f \phi + (\rho c_p)_s (1 - \phi)\} \frac{\partial \langle \overline{T} \rangle^i}{\partial t} + (\rho c_p)_f \nabla \cdot (\mathbf{u}_D \langle \overline{T} \rangle^i)$$

$$= \nabla \cdot \{[k_f \phi + k_s (1 - \phi)] \nabla \langle \overline{T} \rangle^i\} + \nabla \cdot \underbrace{\left[\frac{1}{\Delta V} \int_{A_i} \mathbf{n}(k_f \overline{T_f} - k_s \overline{T_s}) dS\right]}_{\text{I}}$$

$$- (\rho c_p)_f \nabla \cdot \left[\phi \left(\underbrace{\overline{\langle \mathbf{u}' \rangle^i \langle T_f' \rangle^i}}_{\text{II}} + \underbrace{\langle {}^i \overline{\mathbf{u}} \, {}^i \overline{T_f} \rangle^i}_{\text{III}} + \underbrace{\langle \overline{{}^i \mathbf{u}' \, {}^i T_f'} \rangle^i}_{\text{IV}}\right)\right] \qquad (22)$$

As seen above in the two-energy equation model, in order to apply Eq. (22) the underscored terms have to be modeled. To accomplish this, a gradient type diffusion model is used for all the terms, i.e., tortuosity (I), turbulent heat flux due to temporal fluctuations (II), thermal dispersion due to spatial deviations (III), and turbulent thermal dispersion due to temporal fluctuations and spatial deviations (IV).

Therefore, using similar gradient type diffusion models as before, we can write

$$\text{Tortuosity:} \qquad \left[\frac{1}{\Delta V} \int_{A_i} \mathbf{n}(k_f \overline{T_f} - k_s \overline{T_s}) dS\right] = \mathbf{K}_{\text{tor}} \cdot \nabla \langle \overline{T} \rangle^i \qquad (23)$$

$$\text{Turbulent heat flux:} \qquad - (\rho c_p)_f (\phi \overline{\langle \mathbf{u}' \rangle^i \langle T_f' \rangle^i}) = \mathbf{K}_t \cdot \nabla \langle \overline{T} \rangle^i \qquad (24)$$

$$\text{Thermal dispersion:} \qquad - (\rho c_p)_f (\phi \langle {}^i \overline{\mathbf{u}} \, {}^i \overline{T_f} \rangle^i) = \mathbf{K}_{\text{disp}} \cdot \nabla \langle \overline{T} \rangle^i \qquad (25)$$

$$\text{Turbulent thermal dispersion:} \qquad - (\rho c_p)_f (\phi \langle \overline{{}^i \mathbf{u}' \, {}^i T_f'} \rangle^i) = \mathbf{K}_{\text{disp},t} \cdot \nabla \langle \overline{T} \rangle^i \qquad (26)$$

For the above shown expressions, Eq. (22) can be rewritten as

$$\{(\rho c_p)_f \phi + (\rho c_p)_s (1 - \phi)\} \frac{\partial \langle \overline{T} \rangle^i}{\partial t} + (\rho c_p)_f \nabla \cdot (\mathbf{u}_D \langle \overline{T} \rangle^i) = \nabla \cdot \{\mathbf{K}_{\text{eff}} \cdot \nabla \langle \overline{T} \rangle^i\} \qquad (27)$$

where $\mathbf{K}_{\text{eff}}$ given by

$$\mathbf{K}_{\text{eff}} = \underbrace{[\phi k_f + (1 - \phi) k_s]}_{k_{\text{eff}}} \mathbf{I} + \mathbf{K}_{\text{tor}} + \mathbf{K}_t + \mathbf{K}_{\text{disp}} + \mathbf{K}_{\text{disp},t} \qquad (28)$$

is the effective overall conductivity tensor.

Turbulence

In order to apply Eqs. (18) and (19) for the two-energy equation model (2EEM) or Eq. (27) for the one-energy equation model (1EEM), it is necessary to determine the components of the effective conductivity tensors in Eq. (20), i.e., $\mathbf{K}_{f,s}$, $\mathbf{K}_t$, $\mathbf{K}_{\text{disp}}$, and $\mathbf{K}_{\text{disp},t}$ for the 2EEM, and $\mathbf{K}_{\text{tor}}$, $\mathbf{K}_t$, $\mathbf{K}_{\text{disp}}$, and $\mathbf{K}_{\text{disp},t}$ in Eq. (28)

for the 1EEM. Here, for simplicity, all mechanisms are neglected except turbulence, which is explicitly accounted for here (see references [49–51] for a discussion on the determination of such coefficients).

The turbulent heat flux and turbulent thermal dispersion terms $\mathbf{K}_t$ and $\mathbf{K}_{\mathrm{disp},t}$, are modeled through the Eddy diffusivity concept as

$$\mathbf{K}_t + \mathbf{K}_{\mathrm{disp},t} = \phi(\rho c_p)_f \frac{\nu_{t_\phi}}{\sigma_T}\mathbf{I} \tag{29}$$

where $\sigma_T = 0.9$ is the macroscopic turbulent Prandtl number for the fluid energy equation.

Interfacial Heat Transfer, h_i

Wakao et al. [17] proposed a correlation for h_i for a closely packed bed and compared results with their experimental data. This correlation reads,

$$\frac{h_i D}{k_f} = 2 + 1.1 \mathrm{Re}_D^{0.6} \mathrm{Pr}^{1/3} \tag{30}$$

Kuwahara et al. [18] also obtained the interfacial convective heat transfer coefficient for laminar flow as follows.

$$\frac{h_i D}{k_f} = \left(1 + \frac{4(1-\phi)}{\phi}\right) + \frac{1}{2}(1-\phi)^{1/2}\mathrm{Re}_D\,\mathrm{Pr}^{1/3} \quad \text{valid for } 0.2 < \phi < 0.9 \tag{31}$$

Equation (31) is based on porosity dependency and is valid for packed beds of particle diameter D. Following this same methodology, in which the porous medium is considered an infinite number of solid square rods, Saito and de Lemos [49] proposed a correlation for obtaining the interfacial heat transfer coefficient for turbulent flow as,

$$\frac{h_i D}{k_f} = 0.08\left(\frac{\mathrm{Re}_D}{\phi}\right)^{0.8}\mathrm{Pr}^{1/3} \quad \text{for } 1.0 \times 10^4 < \frac{\mathrm{Re}_D}{\phi} < 2.0 \times 10^7 \quad \text{valid for } 0.2 < \phi < 0.9 \tag{32}$$

Nondimensional Parameters

The local Nusselt number for the one-energy equation model used in reference [42] is given by

$$\mathrm{Nu} = \left(\frac{\partial \langle \overline{T} \rangle^i}{\partial y}\right)_{y=H}\frac{H}{T_1 - T_0} \tag{33}$$

Equation (33) assumes the local thermal equilibrium hypothesis, i.e., $\langle T \rangle^i = \langle T_s \rangle^i = \langle T_f \rangle^i$. When the local nonthermal equilibrium model is applied, there are distinct definitions for the Nusselt number associated to each phase, as follows [52].

Fluid phase Nusselt number

$$\mathrm{Nu}_f = \left(\frac{\partial \langle \overline{T}_f \rangle^i}{\partial y}\right)_{y=H} \frac{H}{T_1 - T_0} \tag{34}$$

Solid phase Nusselt number

$$\mathrm{Nu}_s = \left(\frac{\partial \langle \overline{T}_s \rangle^i}{\partial y}\right)_{y=H} \frac{H}{T_1 - T_0} \tag{35}$$

4. NUMERICS

Equations (1), (2), and (18), subject to interface and boundary conditions, were discretized in a two-dimensional control volume involving both clear and porous mediums. The finite volumes method was used in the discretization and the SIMPLE algorithm [51, 52] was applied to handle the pressure-velocity coupling. The discretized form of the two-dimensional conservation equation for a generic property φ in permanent regime reads,

$$I_e + I_w + I_n + I_s = S_\varphi \tag{36}$$

where I_e, I_w, I_n, and I_s represent, respectively, the fluxes of φ in the faces east, west, north, and south faces of the control volume and S_φ its source term.

Standard source term linearization is accomplished by using,

$$S_\varphi \approx S_\varphi^{**} \langle \varphi \rangle_p^i + S_\varphi^* \tag{37}$$

Discretization in the x-direction momentum equation gives,

$$S^{*x} = (S_e^{*x})_P - (S_w^{*x})_P + (S_n^{*x})_P - (S_s^{*x})_P + S_P^* \tag{38}$$

$$S^{**\,x} = S_\phi^{**} \tag{39}$$

where S^{*x} is the diffusive part, here treated in an implicit form. The second term, S^{**x}, entails the additional drag forces due to the porous matrix, the last two terms in Eq. (2), which are treated here explicitly.

5. RESULTS AND DISCUSSION

Input Parameters

For an impinging jet, the flow is considered to be turbulent for Re > 1,000, with the Reynolds number given by

$$\mathrm{Re} = \frac{\rho v_0 D_h}{\mu} \tag{40}$$

Table 1. Input parameters for turbulent flow simulations

Fluid	Density ρ	Viscosity μ	B	L	T_0	T_1	Length scale, ℓ	Turbulence intensity, I
Air	1.225 kg/m^3	1.789×10^{-5} N·s/m^2	14.23 mm	500 mm	309.1 K	347.6 K	0.07B	2%

where v_0 is the incoming jet velocity and $D_h = B$ when calculating Re for adequate comparisons with similar simulations in the literature (see Figure 1).

The low Re turbulence model presented above was used in all simulations to follow. In order to guarantee that grids nodes are positioned within the laminar sub-layer, the closest grid node to the wall had a value for its wall coordinate y^+ less than unity ($y^+ \leq 1$). Further, inlet value for the turbulent kinetic energy k at the jet entrance was estimated using

$$k_0 = \frac{3}{2}(v_0 I)^2 \qquad (41)$$

where I is the turbulence intensity assumed to prevail in the incoming flow. For the dissipation rate of k and ε, the inlet value was calculated according to

$$\varepsilon_0 = c_\mu^{3/4} \frac{k^{3/2}}{\ell} \qquad (42)$$

where ℓ is a length scale associated with the energy containing eddies. Table 1 summarizes the parameters used as input.

Grid Independence Studies

Grid validation was conducted with the conditions Re = 10,400 and $H/B = 2.6$, and for an empty channel (Figure 1a). At the jet entrance, values in Table 1 were employed. For grid independence studies the overall heat power at the impinged wall, given by

$$Q_w = \int_{x=o}^{x=L} -q''\bigg|_{y=H} w\,dx, \quad q''\bigg|_{y=H} = -k_f \left(\frac{\partial \langle \overline{T} \rangle^i}{\partial y}\right)_{y=H} \qquad (43)$$

where $w = 1$ m is the transverse plate width, was calculated for several grids, and compared in Table 2.

Table 2. Influence of grid size on integral wall heat flux

Grid size	40×216	80×216	80×400
Wall heat power Q_w, Eq. (43)	772.75 W	818.87 W	825.68 W
Deviation in relation to grid 80×400	6.41%	0.82%	0.00%

Also, as grid independency studies herein considered an empty channel only the local Nu number along that wall was evaluated with Eq. (33).

Figure 2a shows local Nu distribution calculated according to Eq. (33), also as a function of grid size. One can note in the table that for grids greater than 80×216,
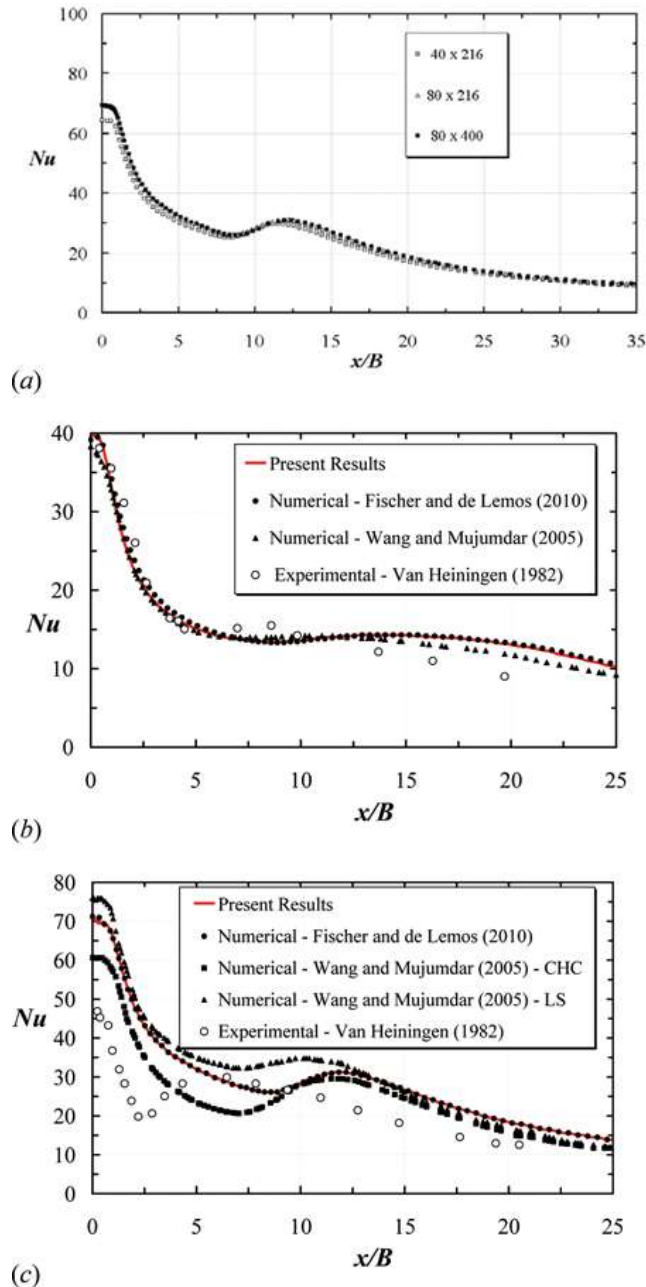

Figure 2. Validation for distribution of Nu along the lower plate for clear channel: (*a*) Effect of grid size, (*b*) $Re = 5,200$, $H/B = 6$, experiments by Van Heiningen (1982) reported by reference [54]; and (*c*) $Re = 10,400$, $H/B = 2.6$, low Re models by Chang et al. (CHS) and Launder and Sharma (LS) reported by reference [55] (color figure available online).

the deviation in relation to the finest grid is less than 1.0%. As such, all simulation for turbulent flow herein were carried out on a grid of size 80×216 (Figure 2a), which was refined close to the wall and about the jet entrance, where the steepest temperature gradients are expected to occur.

Empty Channel

Here, the first set of results is related to the configuration shown in Figure 1a, where an empty channel is analyzed. Once an appropriate grid was chosen, code validation was carried out by comparing Nu numbers calculated at the bottom wall compared with results by Wang and Mujumdar [54] for two cases: $H/B = 6$ and $Re = 5,200$ (Figure 2b), and for $H/B = 2.6$ and $Re = 10,400$ (Figure 2c). The figure indicates that for $H/B = 6$ a good agreement is obtained, whereas for $H/B = 2.6$ results do not match experimental values very well. This might be due to the fact that such flow entails a high degree of complexity, particularly for turbulent flow regime as discussed by Wang and Mujumdar [54] and Heyerichs and Pollard [55]. Nevertheless, as the main purpose of this work is to investigate the influence of a porous layer on heat transfer and not the turbulence model employed, and considering further the fact that a reasonable agreement with experimental data was achieved, the computer code and the grid size were assumed to be sufficiently accurate for the investigation conducted here. Results in Figure 2 are also in agreement with those given by Fischer and de Lemos [42].

Channel with Porous Layer

When a layer of porous material is added to the bottom of the channel, the resulting configuration is shown in Figure 1b. The material is assumed to be rigid, with porosity ϕ, nondimensional thickness h/H, Darcy number $Da = K/H^2$, and thermal conductivity ratio k_s/k_f. Results below are obtained using various Re numbers and distinct values for the four parameters just mentioned.

Effect of Reynolds Re. The Reynolds number was varied from $Re = 10,400$ to $Re = 60,000$, and results were obtained for $H/B = 2.6$, $k_s/k_f = 10$, $Da = 8.95 \times 10^{-5}$, and $h/H = 0.50$.

Figure 3a shows streamlines and indicates that as the Reynolds number increases, the strength of the penetrating flow is sufficiently high to damp recirculation flow outside the porous material as more fluid flows though the permeable medium. Thin boundary layers occur not only around the jet exit but also at the stagnation region for high Re. Figure 3b shows corresponding results for the turbulent kinetic energy. The higher the Reynolds number is, the higher the turbulent kinetic energy on the clear gap and inside the porous medium as well, a feature that is in accordance with results by Graminho and de Lemos [38].

Temperature profiles for the fluid and solid are presented in Figures 3c and 3d, respectively. As the Reynolds number increases, the thermal boundary layer along the hot wall decreases, pushing high temperature isotherms close to the lower wall. It is also interesting to emphasize the bulging of isotherms at around $x/B = 7$ ($x = 0.1$ m), corresponding to a position of nearly stagnant flow. Past such a position,
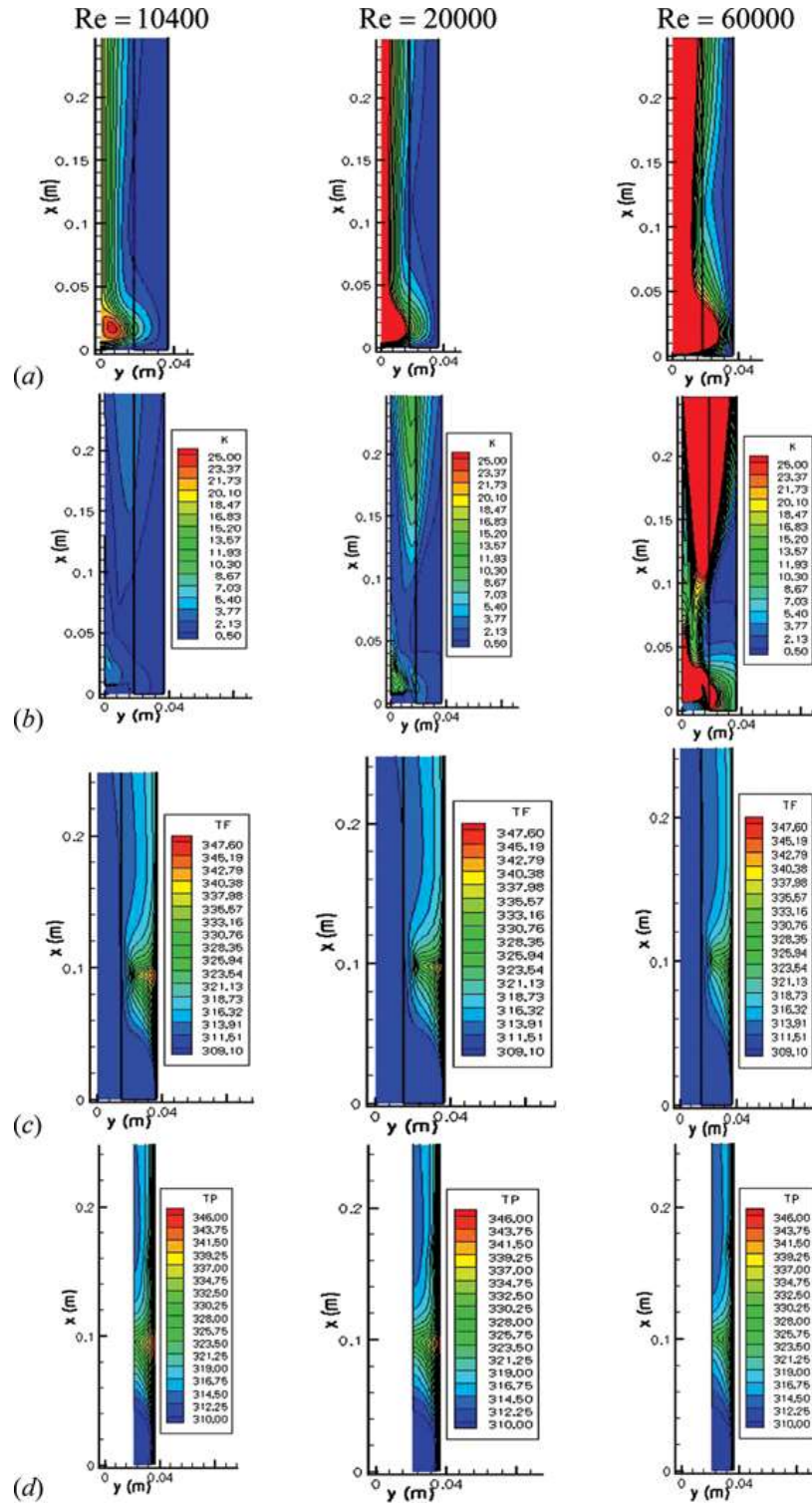
Figure 3. Effect of Re for $H/B = 2.6$, $k_s/k_f = 10$, $Da = 8.95 \times 10^{-5}$, $h/H = 0.50$. (*a*) streamlines, (*b*) turbulent kinetic energy, (*c*) fluid temperature, and (*d*) solid temperature (color figure available online).
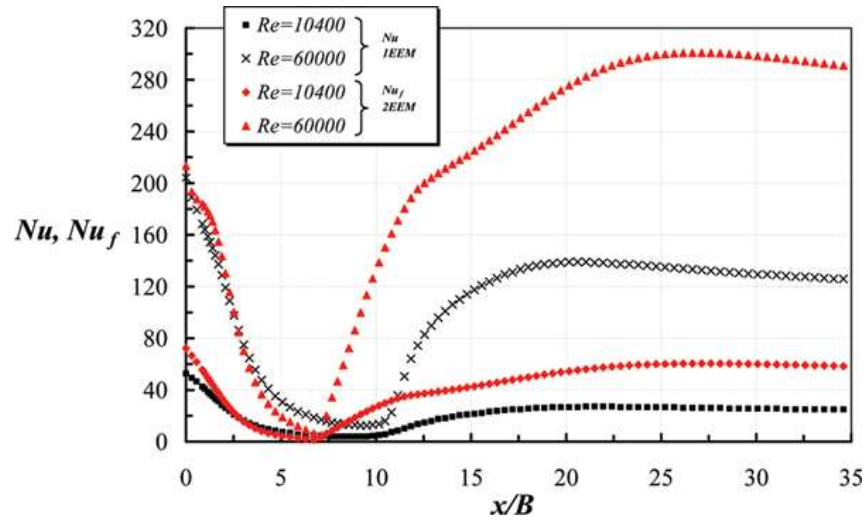
Figure 4. Local Nusselt distribution as a function of the energy model for various Reynolds number. 1EEM = One energy equation model, and 2EEM = two energy equation model, with $Da = 8.95 \times 10^{-5}$, $H/B = 2.6$, $k_s/k_f = 10$, and $h/H = 0.50$ (color figure available online).

the flow accelerates further reducing the thermal boundary layer thicknesses and enhancing temperature gradients at the lower wall.

Figure 4 shows corresponding effects of Re on Nu, calculated for both energy models. It is observed that for low Reynolds number, similar results with one and two energy equation models are obtained since for low Re the energy exchange between solid and fluid phase is lower when compared with high Reynolds number cases. As a consequence, the assumption of a local thermal equilibrium hypothesis becomes more realistic for low Re flows where small convective currents promote less exchange of heat between phases. On the other hand, for high Reynolds number flows, the heat exchanged between phases becomes important and a substantially different local Nusselt is calculated depending on the model applied. Also worth mentioning is the position of minimum $Nu_f(x/B = 7)$, corresponding to the position of bulging of isotherms mentioned earlier in describing Figures 3c and *3d*.

Effect of porosity φ. Here, results were obtained using $H/B = 2.6$, $k_s/k_f = 10$, Re = 10,400, $Da = 8.95 \times 10^{-5}$, φ and $h/H = 0.50$.

Figure 5a presents streamlines for various values of φ. One can note that porosity variation does not strongly influence the flow behavior, as also confirmed by turbulent results presented in Fischer and de Lemos [42]. Also seen is that the presence of the porous layer reduces the size of the primary vortex when the flow pattern is compared to clear channel results (the furthest right column in Figure 5).

Figure 5b shows corresponding results for the turbulent kinetic energy. Note that as porosity decreases, turbulent kinetic energy levels increase. High values of k are also encountered around the jet entrance where steep velocity gradients occur. Around the interface, levels of turbulent kinetic energy are also high. This scenario contrasts with the clear channel distribution where most of the turbulence energy is generated in the recirculation zone corresponding to the primary vortex.
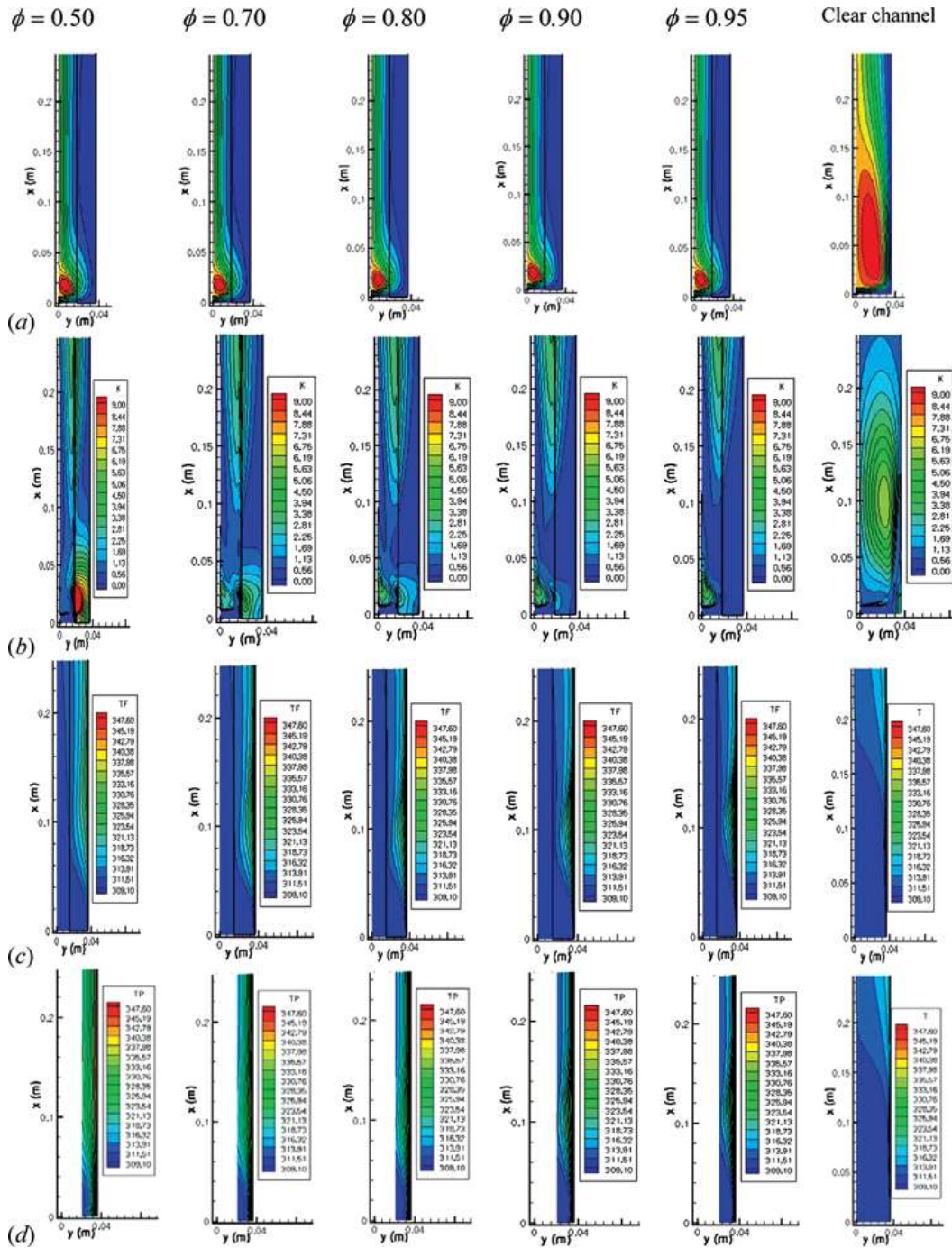
Figure 5. Effect of porosity ϕ for $H/B = 2.6$, $k_s/k_f = 10$, Re = 10,400, Da = 8.95×10^{-5}, and $h/H = 0.50$. (*a*) Streamlines, (*b*) turbulent kinetic energy, (*c*) fluid temperature, and (*d*) solid temperature (color figure available online).

Results for fluid temperatures (Figure 5*c*) seem to indicate that an increase in porosity decreases the thermal boundary layer thickness at the wall, affecting the temperature distribution within the liquid phase with a substantial cooling effect
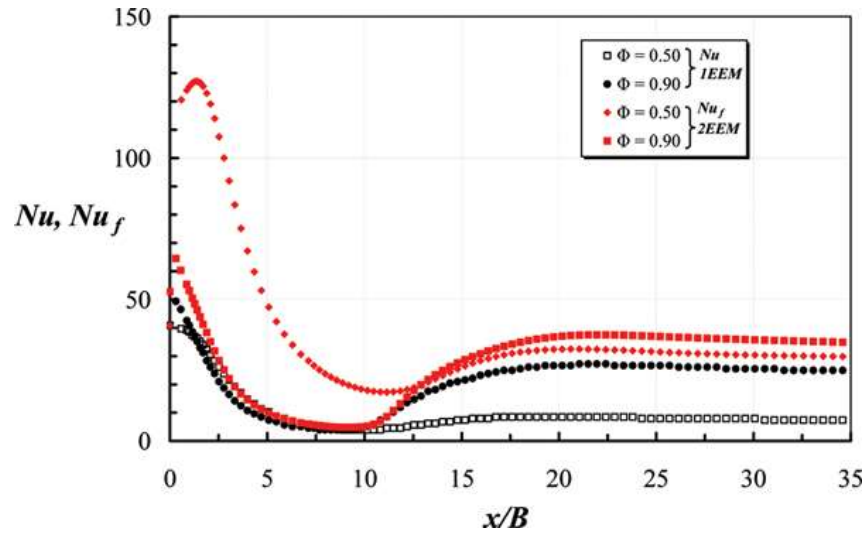
Figure 6. Local Nusselt distribution as a function of the energy model for various porosities with $H/B = 2.6$, $k_s/k_f = 10$, $\text{Re} = 10,400$, $\text{Da} = 8.95 \times 10^{-5}$, and $h/H = 0.50$ (color figure available online).

located at the stagnation region, a result also present in laminar simulations [45]. As ϕ increases, one can also note that as more void space is available for the fluid to permeate through the solid material, cooling of the porous substrate becomes more effective (Figure 5d).

Figure 6 shows the behavior of the local Nusselt number at the bottom wall as a function of energy model and porosity. Local Nusselt distribution calculated with the two models are similar for high porosity cases since in this situation the solid material influence is small. High ϕ values cases are then more realisticly represented with the local thermal equilibrium assumption. On the other hand, for small porosities there are substantial differences in distribution of local Nusselt numbers since those represent cases with more solid material, which, in turn, have a greater impact on the heat exchange between fluid and solid phases. For low porosity cases, consideration of local thermal equilibrium seems to be less realistic.

Effect of channel blockage h/H. A study of the influence of the porous layer thickness and the energy model is now presented. Results are for $H/B = 2.6$, $k_s/k_f = 10$, $\text{Re} = 10,400$, $\text{Da} = 8.95 \times 10^{-5}$, and $\phi = 0.90$.

Figure 7a shows streamlines for several values of h/H. One can note that as the blockage ratio h/H increases, more fluid is forced through the porous material with accompanying reduction of the recirculating bubble in the gap region. The size of the primary vortex is nearly extinguished for $h/H = 0.75$, and streamlines tend to become more uniform within the entire channel.

Turbulent kinetic energy behavior is presented in Figure 7b where maps for k are shown. One can note that as ratio h/H increases, turbulent kinetic energy is generated inside the porous material as well as in the free gap. Additional increase in the blockage ratio forces the flow to be aligned with the macroscopic interface further downstream, leading to high generation rates of k around such an interface. Further increase in h/H pushes the fluid outside the porous material, increasing the velocity
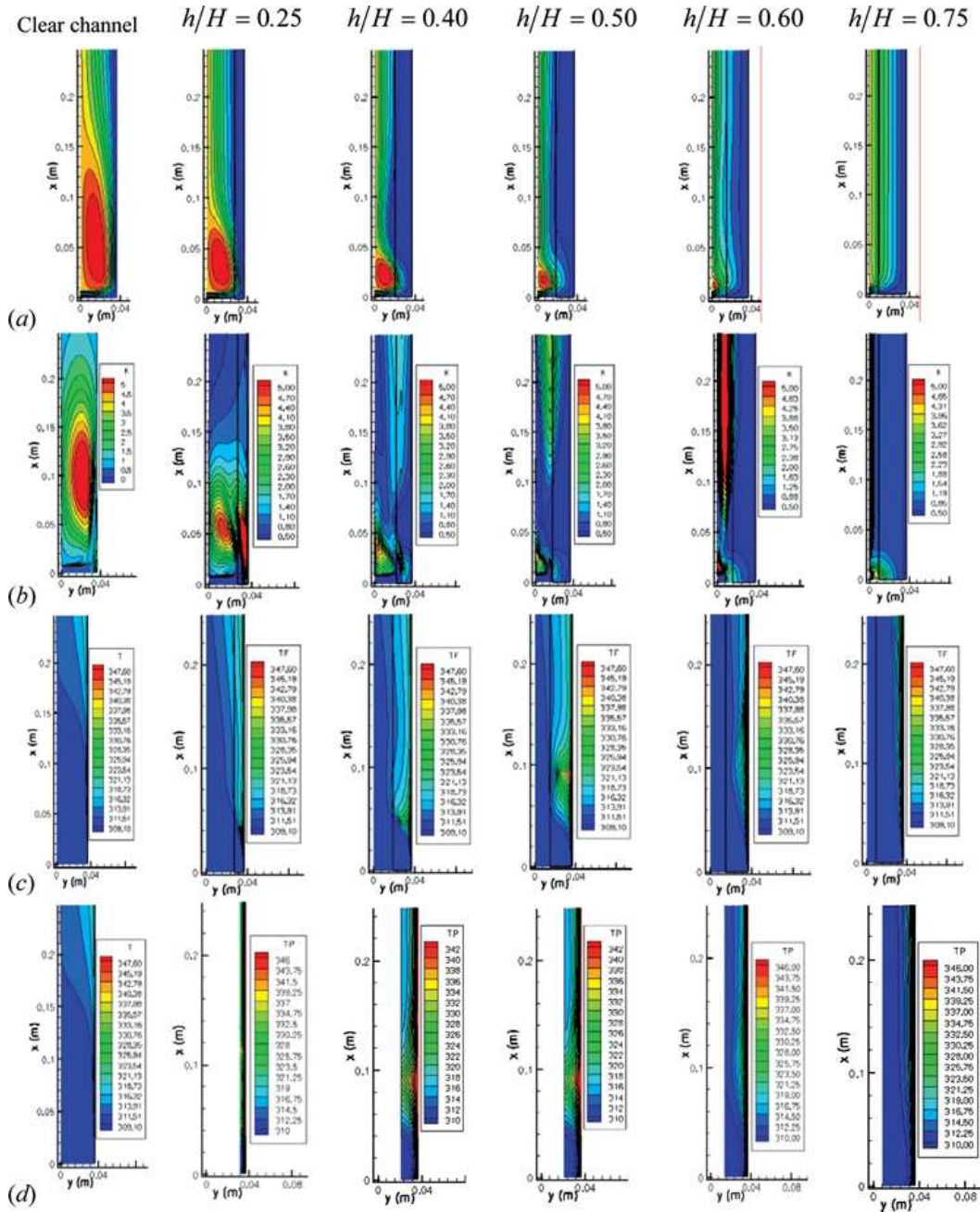
Figure 7. Effect of blockage ratio h/H for $H/B = 2.6$, $k_s/k_f = 10$, $Re = 10,400$, $Da = 8.95 \times 10^{-5}$, and $\phi = 0.90$. (*a*) Streamlines, (*b*) turbulent kinetic energy, (*c*) fluid temperature, and (*d*) solid temperature (color figure available online).

gradient within the free gap, which, in turn, enhances k production rates therein. Effect of h/H on fluid temperatures are shown in Figure 7*c* and show the enlargement of the thermal boundary layer as h/H increases, which presents a peak that moves upstream and is reduced for larger blockage ratio. Corresponding results

for T_s are presented in Figure 7d, which indicates that for low blockage ratios solid and fluid temperatures are quite different, but tend towards equality as thicker porous layers allow for more room for equilibrium between phases to be established.

As in previous plots for Nu, Figure 8a presents Nusselt numbers calculated with the local equilibrium model (1EEM), Eq. (33), with those obtained with the local nonthermal equilibriun model (2EMM), Eq. (34). For thinner porous layers,
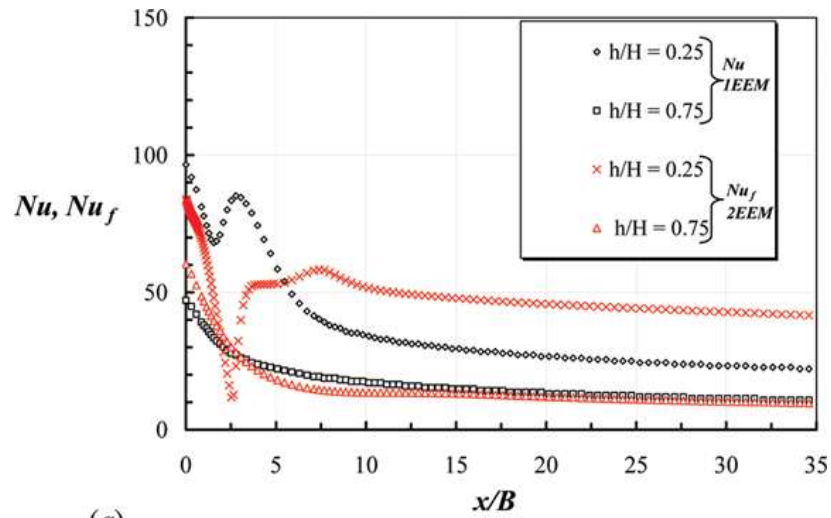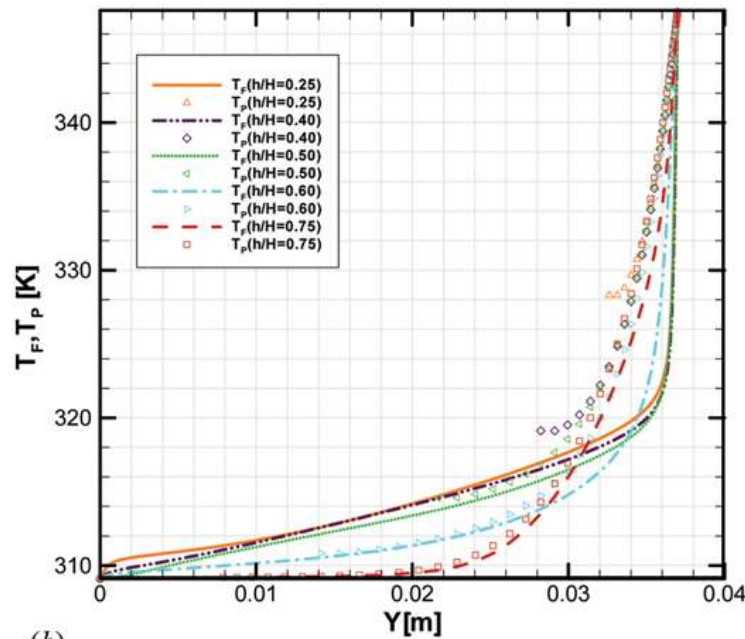
Figure 8. (a) Comparison of axial Nusselt distribution and (b) transversal temperature profiles at $x/B = 25$ for various blockage ratios h/H with, $H/B = 2.6$, $k_s/k_f = 10$, $Re = 10,400$, $Da = 8.95 \times 10^{-5}$, and $\phi = 0.90$. (color figure available online).

both models present a second peak on Nu with and values for it that are substantially different for each model, a reflection of the fact that temperatures for solid and fluid are quite distinct for low h/H values (Figures 7c and 7d). On the other hand, for thicker porous layers models exhibit similar behaviors since in these cases heat exchange between phases is more complete and, as a consequence, temperatures in both phases tend to be equal. Under those conditions, the local thermal equilibrium assumption tends to be more realistic. This observation can be further noted in Figure 8b, which was plotted for the position $x/B = 2.5$, and confirms that for thicker porous layers differences between temperatures of solid and fluid phases are small, leading to similar values for the respective Nusselt numbers. Similar conclusions were drawn by reference [46] for laminar flow, except that here temperature gradients are higher than in laminar flow since in turbulent regime the inter-phase heat exchange, as well as wall heat transfer, are more intense.

Effect of Darcy number Da. Different from what was observed in the analysis of the effects of porosity, permeability does influence the hydrodynamic field, as shown in Figure 9a. Results here are calculated with $H/B = 2.6$, $k_s/k_f = 10$, $Re = 10,400$, $\phi = 0.50$, and $h/H = 0.50$. The primary vortex intensity decreases with a decrease in Da as well as the fluid speed inside the porous layer, which leads to a lower mass flow rate inside the porous substrate. For $Da \leq 2.89 \times 10^{-6}$, the flow nearly vanishes in the porous material as can be seen by the streamlines in Figure 9a.

Figure 9b presents two-dimensional fields for the turbulence kinetic energy, k. For $Da = 7.30 \times 10^{-3}$ and $Da = 3.68 \times 10^{-4}$, generation of k is enhanced and is even grater than for the clear channel case. The region of highest turbulence corresponds to the jet entrance where steep velocity gradients produce high generation rates of k. For very low permeabilities, $Da = 4.86 \times 10^{-7}$, as fluid is pushed to flow thought the clear gap, higher values of k are found around the macroscopic interface between the two media. In addition, high k values are also found due to the small recirculation bubble attached to the jet entrance.

Further, Figure 9c shows temperature distributions for distinct values of $Da = K/H^2$. One can see that as permeability decreases, isothermal lines, referent to the highest temperatures, bulge from the hot wall thickening the thermal boundary layer at the wall surface. Cases with low permeability present fluid temperature peaks at around $x = 0.06$m for $Da = 2.89 \times 10^{-6}$ and $x = 0.04$ m for $Da = 4.86 \times 10^{-7}$. Those peaks seems to be related to flow blockage, which happens earlier along the flow (smaller x/B) as Da is reduced. Corresponding T_s results are found in Figure 9d, where corresponding peaks in the solid temperature can be identified for low permabilites ($Da \leq 2.89 \times 10^{-6}$).

Figure 10 shows Nusselt numbers along the wall as a function of Da, where one can see that in such cases Nu at the stagnation region is most influenced, being reduced as Da is reduced. In the wall jet region, local Nu is also reduced but less intensively when compared with its variation as a function of porosity (Figure 5). Also important to note is that for low Da, Nusselt values using either 1EEM or 2EEM are nearly the same in the developed region ($x/B > 20$), because for very low mass flow rates inside the porous bed, both the solid and fluid temperature gradients at the wall attain nearly the same value giving the same Nu number and validating the so-called thermal equilibrium assumption within the porous material.
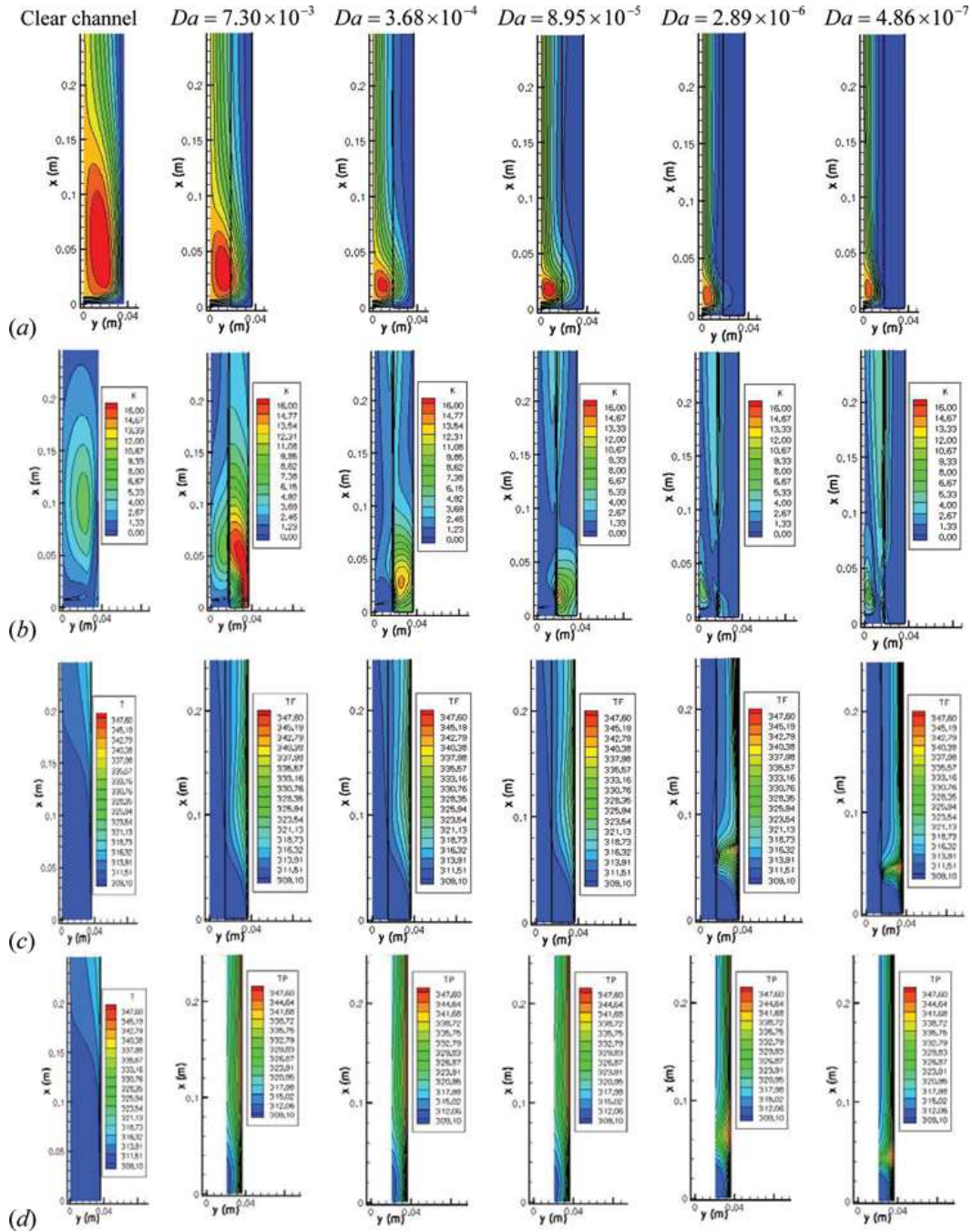
Figure 9. Effect of Da for $H/B = 2.6$, $k_s/k_f = 10$, $Re = 10,400$, $\phi = 0.50$, and $h/H = 0.50$. (a) Streamlines, (b) turbulent kinetic energy, (c) fluid temperature, and (d) solid temperature (color figure available online).

Effect of solid-to-fluid thermal conductivity ratio k_s/k_f. The effect of k_s/k_f on flow and thermal fields is presented in Figure 11, based on the parameters $H/B = 2.6$, $Re = 10,400$, $Da = 8.95 \times 10^{-5}$, $\phi = 0.90$, and $h/H = 0.50$.
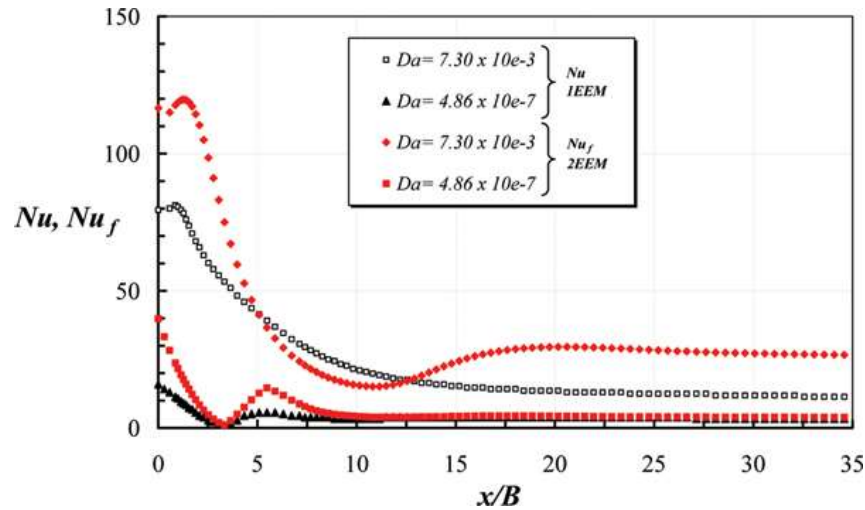
Figure 10. Local Nusselt distribution as a function of the energy model for Darcy number with $H/B = 2.6$, $k_s/k_f = 10$, $Re = 10,400$, $h/H = 0.50$, and $\phi = 0.50$ (color figure available online).

As expected, the mean (Figure 11*a*) and statistical (Figure 11*b*) flow structures are not influenced by the solid-to-fluid thermal conductivity ratio since in the solution methodology applied decoupled formulation was used. Or say, the calculated flow field was not impacted by the thermal field since only constant property cases were run.

Fluid temperatures are presented in Figure 11*c* and indicate that the thermal field is significantly affected by the value of k_s/k_f, as expected. Increasing k_s/k_f reduces the fluid temperature gradient at the wall as a consequence of reducing the solid temperate at corresponding locations (Figure 11*d*). High k_s/k_f ratios increase solid temperature elsewhere, bringing up fluid temperatures as a result of interfacial heat transfer between phases. Also interesting to note is the result on the thermal filed of the nearly stagnant flow around $x/B = 6.5$, where both the fluid and the solid isotherms depart from the wall, with consequent thickening of thermal boundary layers and reductions of temperature gradients at the wall. Nusselt number results in Figure 12 corroborates such findings. One can see in the figure that for the 1EMM model there is a substantial reduction of Nu as k_s/k_f increases, and that when using the local nonthermal equilibrium hypotheses (2EEM) no such substantial reduction in Nu_f is calculated. Also interesting to see is the reduction on Nu_f, at about $x/B = 6.5$, which reflects the bulging of isotherms seen earlier (Figures 11*c* and 11*d*).

Integral Wall Heat Flux

In an earlier paper [43], is was observed that the overall heat transfer to or from a wall would be an indicator of the effectiveness in using porous layers attached to surfaces. Such overall heat transferred from the lower wall to the flowing fluid can be calculated for both configurations presented in Figure 1, as

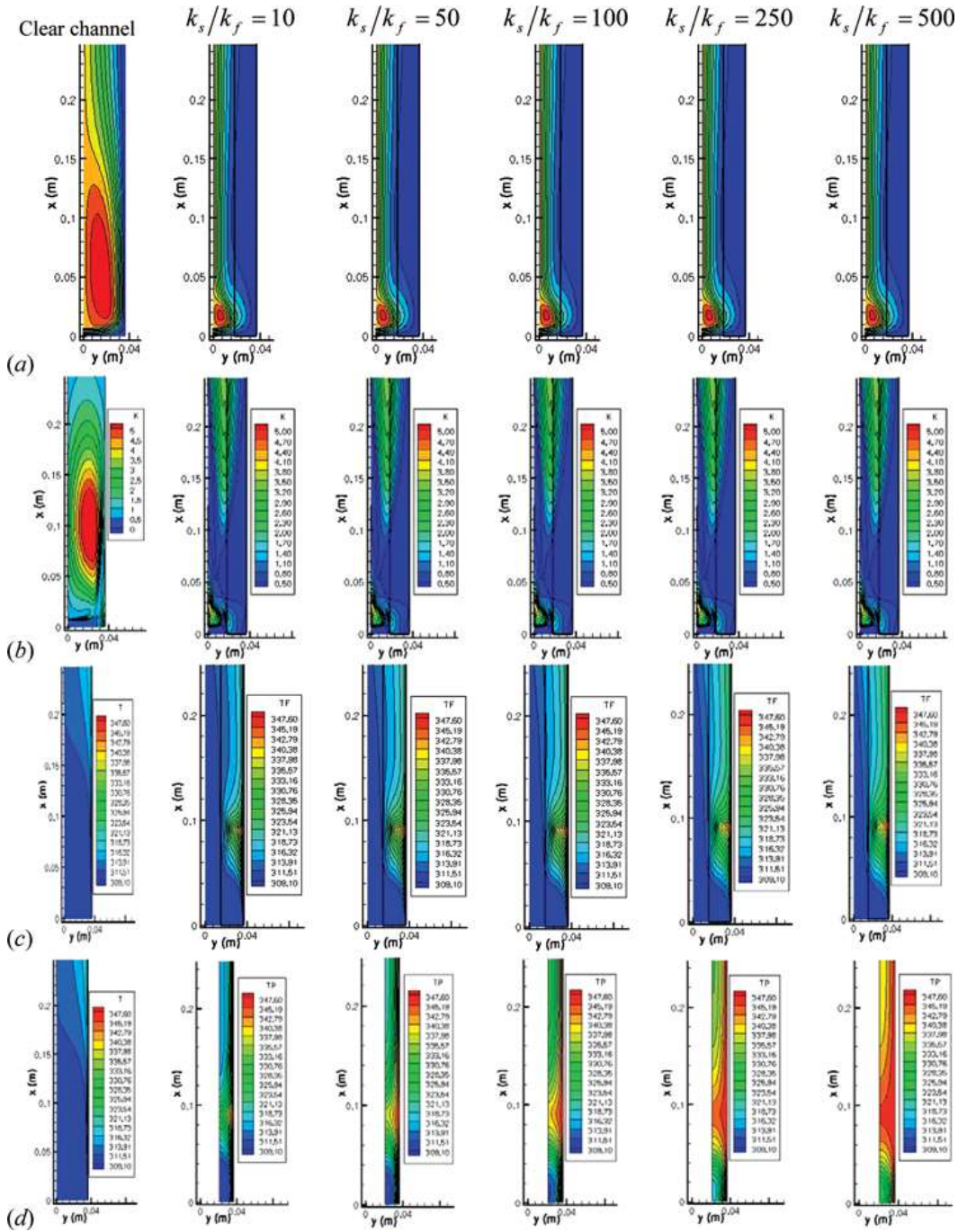$$q_w = \frac{1}{L} \int_o^L q_{wx}(x) dx \qquad (44)$$

Figure 11. Effect of k_s/k_f for $H/B = 2.6$, $\mathrm{Re} = 10{,}400$, $\mathrm{Da} = 8.95 \times 10^{-5}$, $\phi = 0.50$, and $h/H = 0.50$. (*a*) Streamlines, (*b*) Turbulent kinetic energy, (*c*) Fluid Temperature, and (*d*) Solid Temperature (color figure available online).

Depending on the model used, there are two possibilities to evaluate the local wall heat flux q_{wx}. One can use the hypothesis of local thermal equilibrium (LTE or 1EEM), or else individual terms can be applied in each phase in order to calculate the
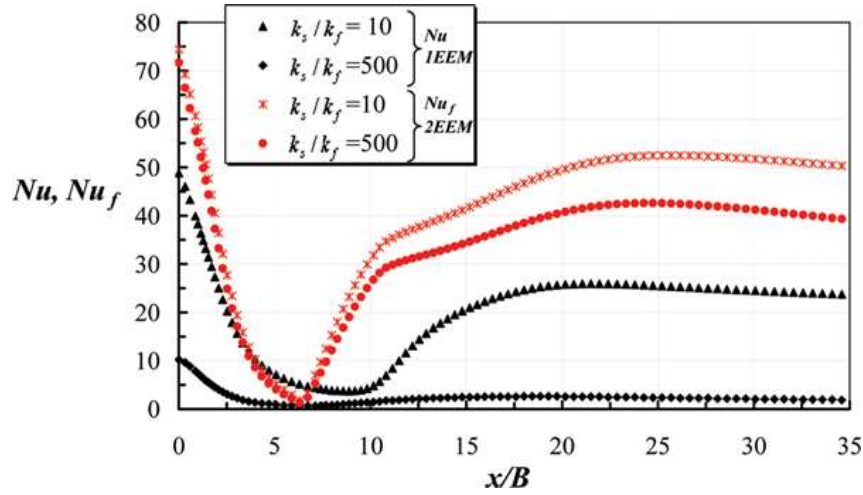
Figure 12. Local Nusselt distribution as a function of the energy model for various ratios of k_s/k_f with $H/B = 2.6$, $\mathrm{Re} = 10{,}400$, $\mathrm{Da} = 8.95 \times 10^{-5}$, $\phi = 0.90$, and $h/H = 0.50$ (color figure available online).

integrated heat transferred from the bottom wall. In the latter case, the LTNE (2EEM) model is employed.

Therefore, for the one-energy equation model one has

$$q_w = \frac{1}{L}\int_o^L q_{wx}(x)\,dx; \quad q_{wx} = -k_{\mathrm{eff}}\left.\frac{\partial\langle T\rangle^i}{\partial y}\right|_{y=H}; \quad k_{\mathrm{eff}} = \phi k_f + (1-\phi)k_s \qquad (45)$$

and for the two-energy equation model

$$q_w = \frac{1}{L}\int_o^L q_{wx}(x)\,dx; \quad q_{wx} = -\left[k_{\mathrm{eff},f}\left.\frac{\partial\langle T_f\rangle^i}{\partial y}\right|_{y=H} + k_{\mathrm{eff},s}\left.\frac{\partial\langle T_s\rangle^i}{\partial y}\right|_{y=H}\right];$$

$$\begin{cases} k_{\mathrm{eff},f} = \phi k_f \\ k_{\mathrm{eff},s} = (1-\phi)k_s \end{cases} \qquad (46)$$

For the cases where the porous layer is considered, the wall hat flux is given a superscript ϕ on the form q_w^ϕ. The ratio q_w^ϕ/q_w can then be seen as a measure of the effectiveness of using a porous layer for enhancing or damping the amount of heat transferred through the wall. In the results for q_w^ϕ/q_w to follow, solid lines are a representation of simulation with the LTE model (1EEM), whereas LNTE computations are plotted using dashed lines (2EMM).

Figure 13 compares the ratio q_w^ϕ/q_w as a function of ϕ for distinct Re, Da, and h/H with $k_s/k_f = 10$. For high Reynolds number, Figure 13a indicates that using a porous layer is always beneficial to heat transfer when the 2EEM model is applied regardless of the porosity of the medium. The figure also suggests that for cases with high permeabilities (high Da, Figure 13b), there is also a net gain when simulations are computed using either model ($q_w^\phi/q_w > 1$). Figure 13c further suggests that when using the 2EEM model, only highly permeable (high ϕ) and thinner layers (small h/H) favor heat transfer from the wall.
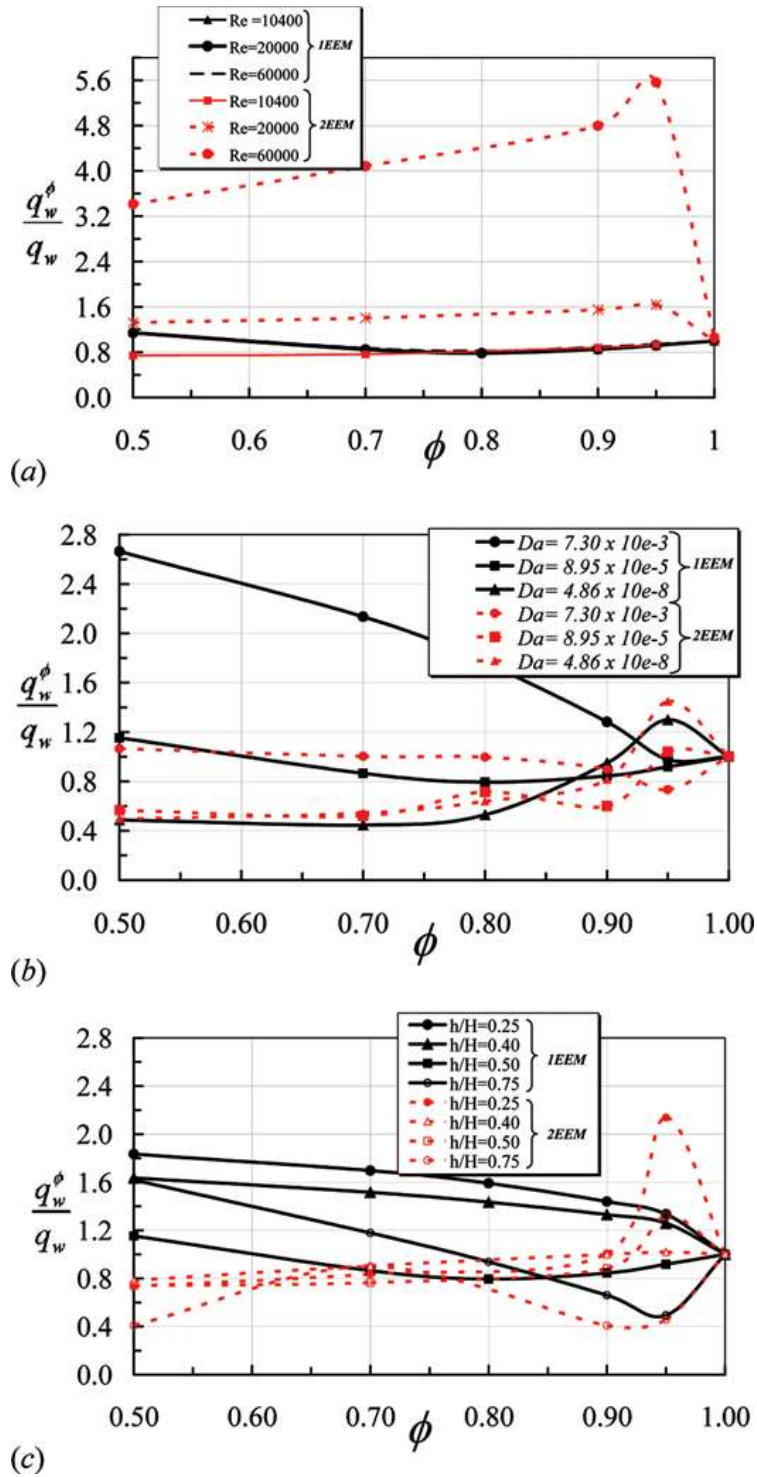
Figure 13. Integral heat flux ratio at the lower wall for varying porosity ϕ, $H/B = 2.6$, and $k_s/k_f = 10$. (a) Effect of Re, (b) effect of Da, and (c) effect of h/H (color figure available online).

Figure 14. Integral heat flux ratio at the lower wall for distinct porosities ϕ with $H/B = 2.6$ and $Re = 10{,}400$. (*a*) Varying h/H, $Da = 8.95 \times 10^{-5}$, $k_s/k_f = 10$; (*b*) Varying Da, $h/H = 0.50$, and $k_s/k_f = 10$; and *c*) varying k_s/k_f, $Da = 8.95 \times 10^{-5}$, and $h/H = 0.5$ (color figure available online).

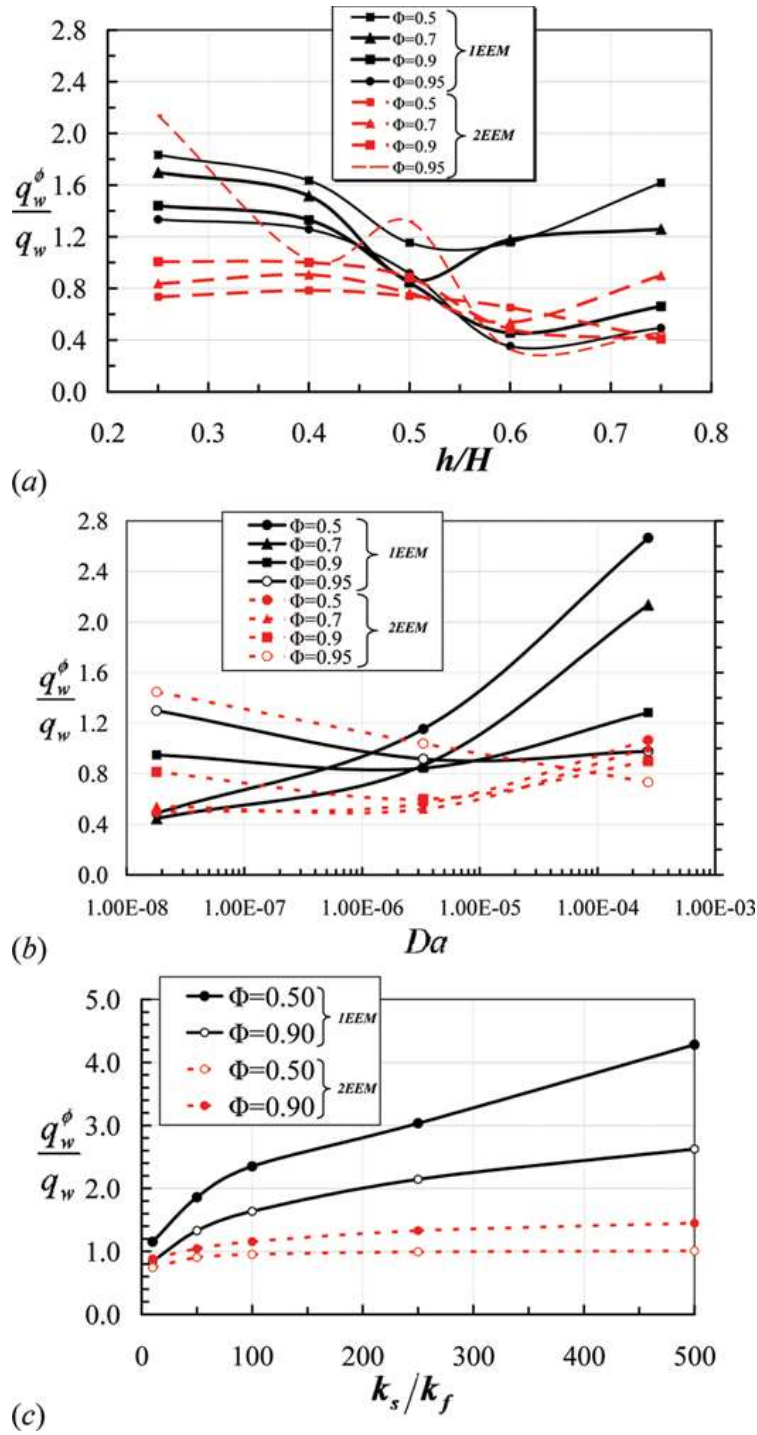Figure 14 further indicates that for thinner porous layers (Figure 14a) and highly permeable materials (Figure 14b), results for q_w^{ϕ}/q_w under the LNTE assumption (dashed lines) give values less than unity, a result that generally contrasts with those by reference [42] who use the LTE approach under the same conditions (solid lines).

Finally, Figure 14c compiles results for q_w^{ϕ}/q_w when the conductivity ratio k_s/k_f is varied. Here, one can notice that only for high porosities and for $k_s/k_f > 50$, both models suggest that the use of a porous layer can always enhance the heat extracted from the bottom wall. The results herein might be useful to design and analysis of energy efficient equipment.

6. CONCLUSION

This work investigated the influence of the presence of a porous layer covering a surface where a jet collides. Two energy modes were applied, namely 1EEM and 2EEM, based, respectively, on the local thermal equilibruim (LTN) and local thermal nonequilibrium hypotheses. It was observed that the Reynolds number and porosity strongly influences the stagnation Nusselt value, while the porous layer thickness affects more intensely the distribution of Nu along the plate. Cases with low porosity and highly permeable layers of porous material tend to yield better heat absorption/release rates when compared with a bare wall case. Regardless of the model used, increasing the thermal conductivity ratio is always beneficial to heat transfer enhancement form the hot wall. Ultimately, results in this work might be useful to engineers designing systems that make use of impinging jets over thermally conducting porous materials.

REFERENCES

1. R. Gardon and J. C. Akfirat, Heat Transfer Characteristics of Impinging Two-Dimensional Air Jets, *J. Heat Transfer*, vol. 101, pp. 101–108, 1966.
2. E. M. Sparrow and T. C. Wong, Impinging Transfer Coefficients due to Initially Laminar Slot Jets, *Int. J. Heat and Mass Transfer*, vol. 18, pp. 597–605, 1975.
3. M. Chen, R. Chalupa, A. C. West, and V. Modi, High Schmidt Mass Transfer in a Laminar Impinging Slot Jet, *Int. J. Heat and Mass Transfer*, vol. 43, pp. 3907–3915, 2000.
4. V. A. Chiriac and A. Ortega, A Numerical Study of the Unsteady Flow and Heat Transfer in a Transitional Confined Slot Jet Impinging on an Isothermal Surface, *Int. J. Heat and Mass Transfer*, vol. 45, pp. 1237–1248, 2002.
5. T. Dermircan and H. Turkoglu, The Numerical Analysis of Oscillating Impinging Jets, *Numer. Heat Transfer A*, vol. 58, no. 2, pp. 146–161, 2010.
6. N. Uddin, S. O. Neumann, B. Weigand, B., and A. Younis, Large-Eddy Simulations and Heat-Fux Modeling in a Turbulent Impinging Jet, *Numer. Heat Transfer A*, vol. 55, no. 10, pp. 906–930, 2009.
7. J. E. Jaramillo, C. D. Pérez-Segarra, I. Rodriguez, and A. Oliva, Numerical Study of Plane and Round Impinging Jets using RANS Models, *Numer. Heat Transfer B*, vol. 54, no. 3, pp. 213–237, 2008.
8. M. K. Isman, E. Pulat, A. B. Etemoglu, and M., Can, Numerical Investigation of Turbulent Impinging Jet Cooling of a Constant Heat Flux Surface, *Numer. Heat Transfer A*, vol. 53, no. 10, pp. 1109–1132, 2008.

 9. Y. Zhang, X. F. Peng, and I. Conte, Heat and Mass Transfer with Condensation in Non-Saturated Porous Media, *Numer. Heat Transfer A*, vol. 52, pp. 1081–1100, 2007.

10. M. E. Taskin, A. G. Dixon, and E. H. Stitt, CFD Study of Fluid Flow and Heat Transfer in a Fixed Bed of Cylinders, *Numer. Heat Transfer A*, vol. 52, no. 3, pp. 203–218, 2007.

11. T. Basak, S. Roy, and H. S. Takhar, Effects of Nonuniformly Heated Wall(s) on a Natural-Convection Flow in a Square Cavity Filled with a Porous Medium, *Numer. Heat Transfer A*, vol. 51, no. 10, pp. 959–978, 2007.

12. J. Eriksson, S. Ormarsson, and H. Petersson, Finite-Element Analysis of Coupled Non-linear Heat and Moisture Transfer in Wood, *Numer. Heat Transfer A*, vol. 50, no. 9, pp. 851–864, 2006.

13. V. Bubnovich, L. Henriquez, and N. Gnesdilov, Numerical Study of the Effect of the Diameter of Alumina Balls on Flame Stabilization in a Porous-Medium Burner, *Numer. Heat Transfer A*, vol. 52, no. 3, pp. 275–295, 2007.

14. X. B. Chen, P. Yu, S. H. Winoto, and H. T. Low, Free Convection in a Porous Wavy Cavity Based on the Darcy-Brinkman-Forchheimer Extended Model, *Numer. Heat Transfer A*, vol. 52, no. 4, pp. 377–397, 2007.

15. N. Yucel and R. T. Guven, Forced-Convection Cooling Enhancement of Heated Elements in a Parallel-Plate Channels using Porous Inserts, *Numer. Heat Transfer A*, vol. 51, no. 3, pp. 293–312, 2007.

16. M. Quintard, M. Kaviany, and S. Whitaker, Two-Medium Treatment of Heat Transfer in Porous Media: Numerical Results for Effective Properties, *Adv. in Water Resources*, vol. 20, pp. 77–94, 1997.

17. N. Wakao, S. Kaguei, and T. Funazkri, Effect of Fluid Dispersion Coefficients on Particle-to-Fluid Heat Transfer Coefficients in Packed Bed, *Chem. Eng. Sci.*, vol. 34, pp. 325–336, 1979.

18. F. Kuwahara, M. Shirota, and A. Nakayama, A Numerical Study of Interfacial Convective Heat Transfer Coefficient in Two-Energy Equation Model for Convection in Porous Media, *Int. J. Heat Mass Transfer*, vol. 44, pp. 1153–1159, 2001.

19. L. Betchen, A. G. Straatman, and B. E. Thompson, A Nonequilibrium Finite-Volume Model for Conjugate Fluid/Porous/Solid Domains, *Numer. Heat Transfer A*, vol. 49, no. 6, pp. 543–565, 2006.

20. Y. W. Zhang, Nonequilibrium Modeling of Heat Transfer in a Gas-Saturated Powder Layer Subject to a Short-Pulsed Heat Source, *Numer. Heat Transfer A*, vol. 50, no. 6, pp. 509–524, 2006.

21. C. R. Ruivo, J. J. Costa, and A. R. Figueiredo, Analysis of Simplifying Assumptions for the Numerical Modeling of the Heat and Mass Transfer in a Porous Desiccant Medium, *Numer. Heat Transfer A*, vol. 49, no. 9, pp. 851–872, 2006.

22. F. Moukalled and Y. Saleh, Heat, and Mass Transfer in Moist Soil, Part I. Formulation and Testing, *Numer. Heat Transfer A*, vol. 49, no. 5, pp. 467–486, 2006.

23. X. H. Wang, M. Quintard, and G. Darche, Adaptive Mesh Refinement for One-Dimensional Three-Phase Flow with Phase Change in Porous Media, *Numer. Heat Transfer B*, vol. 50, no. 3, pp. 231–268, 2006.

24. X. H. Wang, M. Quintard, and G. Darche, Adaptive Mesh Refinement for One-Dimensional Three-Phase Flow with Phase Change in Porous Media, *Numer. Heat Transfer A*, vol. 50, no. 4, pp. 315–352, 2006.

25. A. Mansour, A. Amahmid, M. Hasnaoui, and M. Bourich, Multiplicity of Solutions Induced by Thermosolutal Convection in a Square Porous Cavity Heated from Below and Submitted to Horizontal Concentration Gradient in the Presence of Soret Effect, *Numer. Heat Transfer A*, vol. 49, no. 1, pp. 69–94, 2006.

26. A. V. Kuznetsov, L. Cheng, and M. Xiong, Effects of Thermal Dispersion and Turbulence in Forced Convection in a Composite Parallel-Plate Channel: Investigation of Constant

Wall Heat Flux and Constant Wall Temperature Cases, *Numer. Heat Transfer A*, vol. 42, no. 4, pp. 365–383, 2002.

27. B. M. D. Miranda and N. K. Anand, Convective Heat Transfer in a Channel with Porous Baffles, *Numer. Heat Transfer A*, vol. 46, no. 5, pp. 425–452, 2004.

28. N. B. Santos and M. J. S. de Lemos, Flow and Heat Transfer in a Parallel-Plate Channel with Porous and Solid Baffles, *Numer. Heat Transfer A*, vol. 49, no. 5, pp. 471–494, 2006.

29. M. Assato, M. H. J. Pedras, and M. J. S. de Lemos, Numerical Solution of Turbulent Channel Flow Past a Backward-Facing-Step with a Porous Insert using Linear and Nonlinear k-ε Models, *J. Porous Media*, vol. 8, no. 1, pp. 13–29, 2005.

30. S. Y. Kim and A. V. Kuznetsov, Optimization of Pin-Fin Heat Sinks using Anisotropic Local Thermal Nonequilibrium Porous Model in a Jet Impinging Channel, *Numer. Heat Transfer A*, vol. 44, no. 8, pp. 771–787, 2003.

31. P. Xiang, A. V. Kunetsov, and A. M. Seyam, A Porous Medium Model Hydroentanglement Process, *J. Porous Media*, vol. 11, pp. 35–49, 2008.

32. P. Xiang and A. V. Kunetsov, Simulation of Shape Dynamics of a Long Flexible Fiber in a Turbulent Flow in the Hydroentanglement Process, *Int. Comm. in Heat and Mass Transfer*, vol. 35, pp. 529–534, 2008.

33. M. Prakash, F. O. Turan, Y. Li, J. Manhoney, and G. R. Thorpe, Impinging Round Jet Studies in a Cylindrical Enclosure with and without a Porous Layer, Part I: Flow Visualizations And Simulations, *Chem. Eng. Sci.*, vol. 56, pp. 3855–3878, 2001.

34. M. Prakash, F. O. Turan, Y. Li, J. Manhoney, and G. R. Thorpe, Impinging Round Jet Studies in a Cylindrical enclosure with, and without a Porous Layer, Part II: DLV Measurements and Simulations, *Chem. Eng. Sci.*, vol. 56, pp. 3879–3892, 2001b.

35. W.-S Fu and H.-C. Huang, Thermal Performance of Different Shape Porous Blocks under an Impinging Jet, *Int. J. Heat and Mass Transfer*, vol. 40, no. 10, pp. 2261–2272, 1997.

36. T.-Z. Jeng and S.-C. Tzeng, Numerical Study of Confined Slot Jet Impinging on Porous Metallic Foam Heat Sink, *Int. J. Heat and Mass Transfer*, vol. 48, pp. 4685–4694, 2005.

37. D. R. Graminho and M. J. S. de Lemos, Laminar Confined Impinging Jet into a Porous Layer, *Numer Heat Transfer A*, vol. 54, no. 2, pp. 151–177, 2008.

38. D. R. Graminho and M. J. S. de Lemos, Simulation of Turbulent Impinging Jet into a Cylindrical Chamber with and without a Porous Layer at the Bottom, *Int. J. Heat and Mass Transfer*, vol. 52, pp. 680–693, 2009.

39. M. J. S. de Lemos, *Turbulence in Porous Media: Modeling and Applications*, Elsevier, Kidlington, 2006.

40. F. D. Rocamora and Jr. M. J. S. de Lemos, Analysis of Convective Heat Transfer of Turbulent Flow in Saturated Porous Media, *Int. Comm. Heat and Mass Transfer*, vol. 27, no. 6, pp. 825–834, 2000.

41. M. J. S. de Lemos and C. Fischer, Thermal Analysis of an Impinging Jet on a Plate with and without a Porous Layer, *Numer Heat Transfer A*, vol. 54, pp. 1022–1041, 2008.

42. C. Fischer and M. J. S. de Lemos, A Turbulent Impinging Jet on a Plate Covered with a Porous Layer, *Numer. Heat Transfer A*, vol. 58, pp. 429–456, 2010.

43. M. B. Saito and M. J. S. de Lemos, Interfacial Heat Transfer Coefficient for Nonequilibrium Convective Transport in Porous Media, *Int. Comm. in Heat and Mass Transfer*, vol. 32, no. 5, pp. 666–676, 2005.

44. M. B. Saito and M. J. S. de Lemos, A Macroscopic Two-Energy Equation Model for Turbulent Flow and Heat Transfer in Highly Porous Media, *Int. J. Heat and Mass Transfer*, vol. 53, nos. 11–12, pp. 2424–2433, 2010.

45. F. T. Dórea and M. J. S. de Lemos, Simulation of Laminar Impinging Jet on a Porous Medium with a Thermal Nonequilibrium model, *Int. J. Heat and Mass Transfer*, vol. 53, pp. 5089–5101, 2010.

46. W. G. Gray and P. C. Y. Lee, On the Theorems for Local Volume Averaging of Multiphase System, *Int. J. Multiphase Flow*, vol. 12, pp. 401–410, 1977.

47. B. E. Launder and D. B. Spalding, The Numerical Computation of Turbulent Flows, *Comp. Meth. Appl. Mech. Eng.*, vol. 3, pp. 269–289.

48. K. Abe, Y. Nagano, and T. Kondoh, An Improved k-ε Model for Prediction of Turbulent Flows with Separation and Reattachment, *Trans. JSME Ser. B*, vol. 58, no. 554, pp. 3003–3010, 1992.

49. M. B. Saito and M. J. S. de Lemos, A Correlation for Interfacial Heat Transfer Coefficient for Turbulent Flow over an Array of Square Rods, *J. Heat Transfer*, vol. 128, pp. 444–452, 2006.

50. F. Kuwahara and A. Nakayama, Numerical Modeling of Non-Darcy Convective Flow in a Porous Medium, *Proc. 11th Int. Heat Transf. Conf.*, Kyongyu, Korea, vol. 4, pp. 411–416, 1998.

51. A. Nakayama and F. Kuwahara, A Macroscopic Turbulence Model for Flow in a Porous Medium, *J. Fluids Eng.*, vol. 121, pp. 427–433, 1999.

52. B. Alazmi and K. Vafai, Analysis of Variants within the Porous Media Transport Models, *J. Heat Transfer*, vol. 122, pp. 303–326, 2000.

53. S. V. Patankar, *Numerical Heat Transfer and Fluid Flow*, Hemisphere, New York, 1980.

54. S. J. Wang and A. S Mujundar, A Comparative Study of Five Low Reynolds number k–ε Models for Impingement Heat Transfer, *App. Therm. Eng*, vol. 25, pp. 31–44, 2005.

55. K. Heyerichs and A. Pollard, Heat Transfer in Separated and Impinging Turbulent Flows, *Int. J. Heat Mass Transfer*, vol. 39, no. 12, pp. 2385–2400, 1996.